

# Robust and Fast Decoding of High-Capacity Color QR Codes for Mobile Applications

Zhibo Yang, *Student Member, IEEE*, Huanle Xu, Jianyuan Deng,  
Chen Change Loy, *Member, IEEE*, and Wing Cheong Lau, *Senior Member, IEEE*

**Abstract**—The use of color in QR codes brings extra data capacity, but also inflicts tremendous challenges on the decoding process due to chromatic distortion—cross-channel color interference and illumination variation. Particularly, we further discover a new type of chromatic distortion in high-density color QR codes—cross-module color interference—caused by the high density which also makes the geometric distortion correction more challenging. To address these problems, we propose two approaches, namely, LSVM-CMI and QDA-CMI, which jointly model these different types of chromatic distortion. Extended from SVM and QDA, respectively, both LSVM-CMI and QDA-CMI optimize over a particular objective function to learn a color classifier. Furthermore, a robust geometric transformation method is proposed to accurately correct the geometric distortion for high-density color QR codes. We put forth and implement a framework for high-capacity color QR codes equipped with our methods, called HiQ. To evaluate the performance of HiQ, we collect a challenging large-scale color QR code dataset, CUHK-CQRC, which consists of 5390 high-density color QR code samples. The comparison with the baseline method [2] on CUHK-CQRC shows that HiQ at least outperforms [2] by 188% in decoding success rate and 60% in bit error rate. Our implementation of HiQ in iOS and Android also demonstrates the effectiveness of our framework in real-world applications.

**Index Terms**—color QR code, color recovery, color interference, high capacity, high density, robustness, chromatic distortion

## I. INTRODUCTION

IN recent years, QR codes have gained great popularity because of their quick response to scanning, robustness to damage, readability from any directions. However, the data capacity of existing QR codes has severely hindered their applicability, e.g., adding authentication mechanisms to QR codes to protect users from information leakage [3]. To increase the data capacity of QR codes, leveraging color is arguably the most direct and inexpensive approach.

Unfortunately, it remains an open technical challenge to decode color QR codes in a robust manner, especially for high-density ones. The difficulties of increasing the capacity/footprint ratio boil down to two types of distortion which can be further exacerbated for high-density color QR codes. The first distortion is *geometric distortion*: standard QR code decoding algorithms correct geometric distortion via perspective projection [4], which estimates a projection matrix from four spatial patterns (the so-called finder pattern and alignment pattern) in the four corners of the QR codes. In practice, it is very likely that the estimated positions of the

patterns are inaccurate. While small deviation is tolerable when decoding low-density QR codes, perspective projection becomes unreliable for high-density ones as each module (module refers to the small square unit that makes up QR code) only contains few pixels. Consequently, minor errors are amplified and propagated through geometric transformation which ultimately leads to decoding failure.

The other distortion is *chromatic distortion*: For monochrome QR codes, a simple thresholding method is adequate to recover the color since there are only two colors between which the chromatic contrast is often high. However, color recovery for color QR codes, which may consist of 4, 8, or even 16 colors, becomes a non-trivial task due to chromatic distortion. We characterize the chromatic distortion of color QR codes in three different forms based on their physical or optical causes, see Fig. 1 for illustration:

- **Cross-channel interference (CCI).** Colorants in each channel tend to interfere with the colorants in other channels [2], see Fig. 1(a). CCI scatters the distribution of each color, and thus leads to difficulties in differentiating one color from the others;
- **Illumination variation.** Color varies dramatically under different lighting conditions [5] (see Fig. 1(b)), and operating under a wide range of lighting conditions is inevitable for real-world QR code applications;
- **Cross-module interference (CMI).** For high-density color QR codes, the colorants in neighboring data modules may spill over and severely distort the color of the central module, see Fig. 1(c). CMI has negligible influence over low-density color QR codes whose module is large enough because it only occurs along the edges of each module, hardly contaminating the module center over which color recovery is performed.

To the best of our knowledge, CMI has never been studied before and is especially important for decoding high-density color QR codes, while CCI and illumination variation have been addressed by prior arts [2] [6]. To address illumination variation, they take an online approach, namely, they learn a color recovery model for every captured QR code image. However, we have found that online approach brings huge computational burden to mobile devices and it is difficult to collect enough clean training data for high-density color QR codes due to CMI and other external causes, e.g., dirt, damage and nonuniform illumination on the reference symbols from which the training data are collected.

In this paper, we adopt an offline learning approach, and

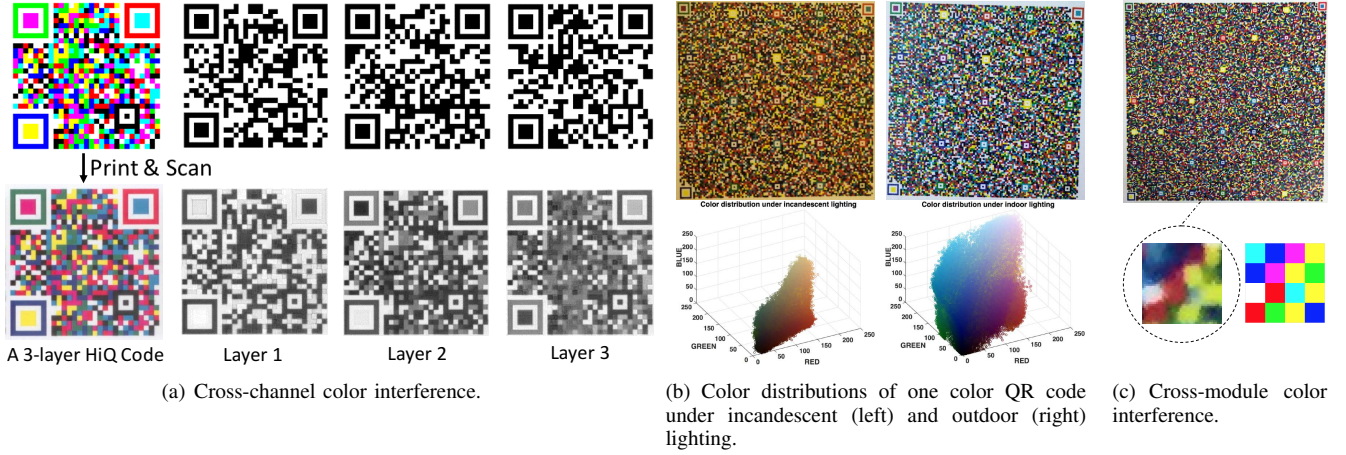


Figure 1: Three types of chromatic distortion of color QR codes.

model the cross-module interference together with the fallout of illumination variation and the cross-channel interference by formulating the color recovery problem with an optimization framework. In particular, we propose two models, QDA-CMI and LSVM-CMI, which are extended from quadratic discriminant analysis (QDA) and support vector machine (SVM), respectively. A robust geometric transformation method is further developed to accurately correct geometric distortion. Besides, we propose a new color QR code framework, HiQ, which constructs a color QR code by combining multiple monochrome QR codes together in a layered manner to maintain the structure of conventional QR codes, and thus to preserve the strength of their design. We refer the color QR codes constructed under HiQ framework as HiQ codes in the remainder of this paper. To summarize, this paper has primarily made the following technical contributions:

- **Chromatic and geometric distortion correction.** To the best of our knowledge, this paper is the first one that discovers the cross-module color interference in high-density QR codes and establishes models to simultaneously correct different types of chromatic distortion. A robust geometric transformation algorithm is also proposed to address the challenge of geometric distortion.
- **Working implementation and applications.** We propose a high-capacity QR code framework, HiQ, which provides users and developers with great flexibility of encoding and decoding QR codes with high capacity. Experimental results show that with HiQ we can encode 2900 bytes, 7700 bytes and 8900 bytes of data in a region as small as  $26 \times 26 \text{ mm}^2$ ,  $38 \times 38 \text{ mm}^2$  and  $42 \times 42 \text{ mm}^2$ , respectively, and robustly decode the data within 3 seconds using off-the-shelf mobile phone. We release our implementation of one HiQ codes generator<sup>1</sup> and two mobile decoders on Apple App Store<sup>2</sup> and Google Play<sup>3</sup>.

- **A large-scale color QR code dataset.** For benchmarking color QR code decoding algorithms, we create a challenging color QR code dataset, CUHK-CQRC<sup>4</sup>, which consists of 5390 samples of color QR codes captured by different mobile phones under different lighting conditions. This is the first large-scale color QR code dataset that is publicly available. We believe many researches and applications will benefit from it.

The remainder of this paper is structured as follows. Section II reviews the existing color 2D barcodes systems and motivates the need for a new color QR code system. Section III describes the construction of a color QR code under the HiQ framework. Section IV and Section V present the details of the proposed models for correcting chromatic distortion and robust geometric transformation, respectively. The implementation details and further optimization of the decoding performance are discussed in Section VI. Section VII compares HiQ with the baseline method [2] on CUHK-CQRC. Our implementations of HiQ in both desktop simulation and actual mobile platforms are described to demonstrate the practicality of the proposed algorithms. Section VIII concludes this paper.

## II. RELATED WORK

Recent years have seen numerous attempts on using color to increase the capacity of traditional 2D barcodes [2] [6] [7] [8] [9] [10] (see Fig. 2 for illustration). Besides, color feature has also been imposed on traditional 2D barcodes purely for the purpose of improving the attractiveness of 2D barcodes such as PiCode [11]. As a real commercial product, Microsoft High Capacity Color Barcode (HCCB) [9], encodes data using color triangles with a predefined color palette. However, A. Grillo et. al. [6] reports fragility in localizing and aligning HCCB codes. The only available HCCB decoder, Microsoft Tag, requires Internet accessibility to support server-based decoding.

Recent projects like COBRA [12], Strata [13] and FOCUS [14] support visual light communications by streaming a sequence of 2D barcodes from a display to the camera of the receiving smartphone. However, the scope of their work

<sup>1</sup>Available at <http://www.authpaper.net/>.

<sup>2</sup>iOS App <https://itunes.apple.com/hk/app/authpaper-qr-code-scanner/id998403254?ls=1&mt=8>.

<sup>3</sup>Android App <https://play.google.com/store/apps/details?id=edu.cuhk.ie.authbarcodescanner.android>.

<sup>4</sup>Available at <http://www.authpaper.net/colorDatabase/index.html>.

is different from ours. They focus on designing new 2D (color or monochrome) barcode systems that are robust for message streaming (via video sequences) between relatively large smartphone screens (or other displays) and the capturing camera. In contrast, our work focuses on tackling the critical challenges such as CMI and CCI to support fast and robust decoding when dense color QR-codes are printed on paper substrate with maximal data-capacity-per-unit-area ratio.

H. Bagherinia and R. Manduchi [15] propose to model the color variation under various illuminations using a low-dimension subspace, e.g., principal component analysis, without requiring reference color patches. T. Shimizu et. al. [16] propose a 64-color 2D barcode and augment the RGB color space using seed colors which functions as references to facilitate color classification. Their method uses 15-dim or 27-dim feature both in training and testing which is prohibitively time-consuming for mobile devices in real-world applications. To decode color barcodes from blurry images, H. Bagherinia and R. Manduchi [17] propose an iterative method to address the blur-induced color mixing from neighboring color patches. However, their method takes more than 7 seconds on a desktop with Intel i5-2520M CPU @ 2.50GHz to process one image, which is completely unacceptable for mobile applications.

Other researchers have extended traditional QR codes to color QR codes to increase their data capacity [2] [6] [10]. HCC2D proposed in [2] encodes multiple data bits in each color symbol and adds extra color symbols around the color QR codes to provide reference data in the decoding process. The per-colorant-channel color barcodes framework (PCCC) [2] encodes data in three independent monochrome QR codes which represent the three channels in the CMY color space during printing. A color interference cancellation algorithm is also proposed in [2] to perform color recovery. However, both HCC2D and PCCC suffer from the following drawbacks:

- parameters of the color recovery model should be learned before decoding for every captured image. Our experiments show such approach not only brings unnecessary computational burden to mobile devices, but also easily introduces bias in the color recovery process since any dirt and damage on the reference symbols, or even nonuniform lighting can easily make color QR codes impossible to decode;
- their evaluations do not study the effectiveness of their proposed schemes on high-density color QR codes<sup>5</sup>, neither do they discover or address the problem of cross-module interference;
- they do not investigate the limitations regarding smartphone-based implementations.

In contrast, our proposed HiQ framework addresses the aforementioned limitations in a comprehensive manner. On the encoding side, HiQ differs from HCC2D in that HiQ codes do not add extra reference symbols around the color QR codes; and the color QR codes generation of PCCC framework is a special case of HiQ, namely, 3-layer HiQ codes. On the decoding side, the differences mainly lie in the geometric

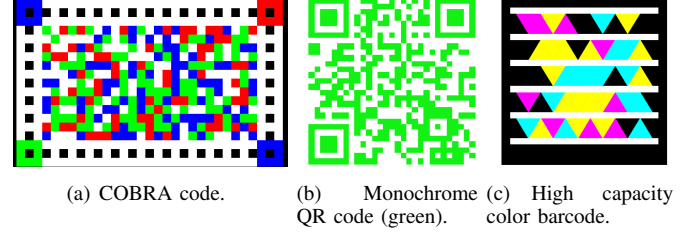


Figure 2: Examples of different types of 2D barcodes.

distortion correction and color recovery. HiQ adopts offline learning, and thus does not use reference color during color recovery as HCC2D and PCCC do. More importantly, by using RGT and QDA-CMI (or LSVM-CMI), HiQ addresses the problem of geometric and chromatic distortion particularly for high-density color QR codes which are not considered by HCC2D or PCCC.

### III. HIQ: A FRAMEWORK FOR HIGH-CAPACITY QR CODES

Fig. 3 gives an overview of the encoding and decoding process of the proposed HiQ framework. To exploit and reuse existing QR code systems, we keep intact the structure of traditional QR codes in our HiQ code design and select a highly discriminable set of colors to transform multiple traditional QR codes into one HiQ code. Specifically, HiQ firstly partitions the data to be encoded into multiple small pieces and encodes them into different monochrome QR codes independently. Note that different layers of monochrome QR codes can have different levels of error correction, but they must have the number of modules in order to preserve the structure of conventional QR codes. Secondly, HiQ uses different colors that are easily distinguishable to represent different combinations of the overlapping modules of the superposed monochrome QR codes. In addition, we paint the spatial patterns with specific colors to provide reference color (whose colors are known beforehand) as well as to carry some format information of the HiQ code, e.g., the number of layers, which can be used in the decoding phase. We use “layer” to denote the monochrome QR codes in a HiQ code hereafter. By this definition, a HiQ code that is comprised of  $n$  monochrome QR codes is called  $n$ -layer HiQ code.

Given  $n$  monochrome QR codes,  $\{M_i\}$ , where  $i = 1, 2, \dots, n$ , each  $M_i$  is composed of the same number of modules. We denote the  $j$ th module of  $M_i$  by  $m_j^i$ , where  $m_j^i = 0$  or  $1$ . In order to achieve layer independence and separability in HiQ codes, HiQ constructs an  $n$ -layer HiQ code  $C_n$  by concatenating all  $M_i$  together so that the  $j$ th module of  $C_n$ ,  $c_j^n = \{m_j^1, m_j^2, \dots, m_j^n\}$ . Then, each  $c_j^n$  is mapped into a particular color using a predefined color codebook  $\mathbb{B}$ , where  $|\mathbb{B}| = 2^n$  as  $m_j^i$  is binary.

An  $n$ -layer HiQ code has a data capacity that is  $n$  times that of a monochrome QR code of the same number of modules. Alternatively, given the same amount of data to carry (within the capacity of a monochrome QR code), HiQ consumes much less substrate footprint in print media than traditional QR code

<sup>5</sup>The color QR samples used by [2] only hold no more than 150 bytes within an area whose size ranges from 15 mm to 30 mm.



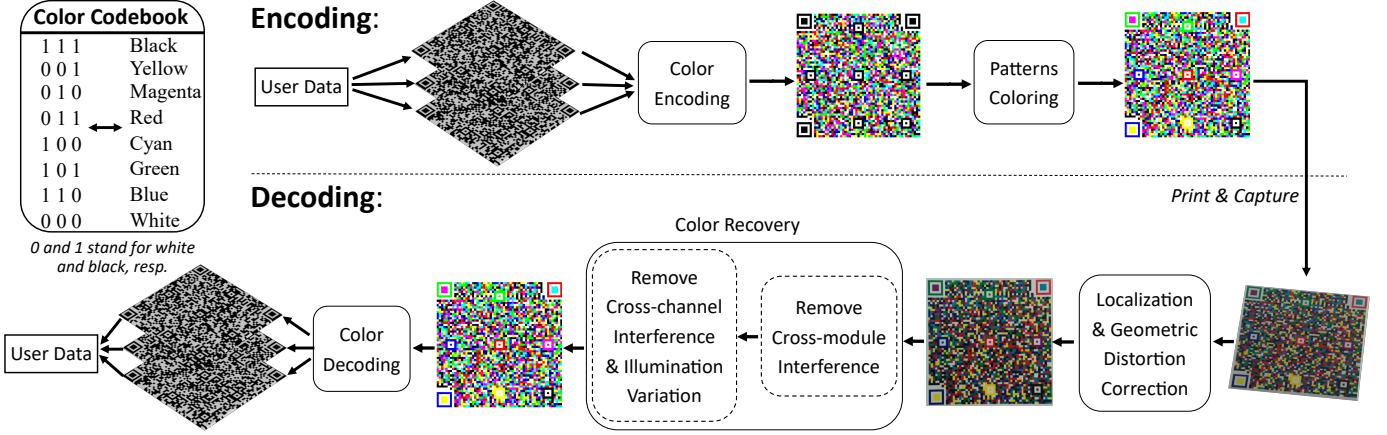


Figure 3: An overview of the encoding and decoding of a 3-layer HiQ code in HiQ.

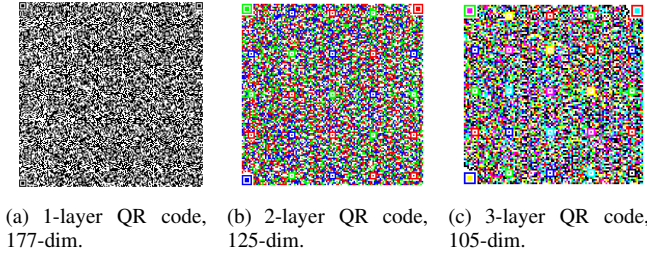


Figure 4: Examples of color QR codes of different layers with the same content size. All layers are protected with a low level of error correction.

does, assuming same printout density. HiQ codes degrade to monochrome QR codes when  $n = 1$ . The color QR code proposed in [2] is also a special case of HiQ with  $n = 3$ . In a nutshell, HiQ is a framework that provides users and developers with more flexibilities in generating QR codes in terms of data capacity, embedded error correction level and appearance (color). Fig. 4 gives examples of HiQ color QR codes of different layers ranging from 1 to 3. Given the same amount of user data and printout size, HiQ codes with fewer layers are denser than those with more layers. However, using more layers sharply increases the number of colors in HiQ codes. Consequently, the difficulty of decoding (mainly color recovery) increases.

#### IV. MODELING CHROMATIC DISTORTION

##### A. Framework Overview

The problem of illumination variations give rise to the so-called color constancy [18] [19] problem which has been an active area of computer vision research. However, most existing algorithms for color constancy tend to be computation-intensive, and thus not viable for our application of HiQ code decoding using off-the-shelf smartphones. To balance between complexity and efficacy, we adopt the method from [5] and normalize the RGB intensities of each sampled pixel with the white color estimated from the QR code image by leveraging the structure of QR codes. This effectively makes the color feature less illumination-sensitive.

Given a captured image of an  $n$ -layer HiQ code, we first estimate the RGB intensities of the white color  $\mathbf{W}$ , of the captured image from white regions in the HiQ codes (e.g., white areas along the boundaries and within spatial patterns). We denote a pixel sampled during geometric transformation<sup>6</sup> by  $(x, y)$ , where  $x$  is a 3-dim color feature and  $y = 1, 2, \dots, 2^n$  being the color label. Instead of directly using RGB intensities,  $\mathbf{I} = \{\mathbf{I}_R, \mathbf{I}_G, \mathbf{I}_B\}$ , as the color feature for color recovery, we normalize  $\mathbf{I}$  by  $\mathbf{W}$ :  $x_j = \mathbf{I}_j / \mathbf{W}_j, j \in \{R, G, B\}$ .

Yet due to the fact that the estimation of white color (i.e.,  $\mathbf{W}$ ) may contain noise, we augment the training data by deliberately injecting noise to  $\mathbf{W}$  to enhance the robustness of the color classifier. More precisely, besides the original data point  $(x, y)$ , each sampled pixel  $\mathbf{I}$  is further normalized by five “noisy” estimations of white color which are randomly and independently drawn from a normal distribution with mean  $\mathbf{W}$  and a small standard deviation. Lastly, given  $x$  as the input, the classifier outputs  $y$  which is then mapped to  $n$  binary bits for decoding using the same color codebook in encoding process.

Contrary to other frameworks such as [2] and [6] which train the classifier online (in real-time) for each captured image, HiQ learns the parameters of the classifier offline using color data collected exhaustively from real-world settings of QR codes scanning. This avoids training bias and unnecessary computations on mobile devices. As one of the most commonly used classification tool in many recognition tasks, Support Vector Machine (SVM), can be used as a color classifier. To train a multi-class SVM, one-vs-one and one-vs-all [20] are the widely-adopted schemes. However, they suffer from the drawback that the decoding process is quite time-consuming: one-vs-one and one-vs-all schemes need  $2^n$  and  $2^{2^n}$  binary classifiers, respectively. Taking advantages of the layered structure in data encoding of HiQ codes, we propose a *layered strategy* where we train a binary SVM for each layer independently to predict the bit in the corresponding layer.

For  $n$ -layer color QR codes, the training data are denoted as  $\{\mathcal{X}, \mathcal{Y}\}$ , where  $\mathcal{X}$  and  $\mathcal{Y}$  are sets of normalized RGB values and binary  $n$ -tuples (e.g.,  $\{1, 0, \dots, 0\}$ ), respectively. Traditional one-vs-all strategy just treats  $\mathcal{Y}$  as color indicators

<sup>6</sup>Our method samples one representative pixel from the central region of each module.

and trains  $2^n$  binary SVMs on  $\{\mathcal{X}, \mathcal{Y}\}$  as there are  $2^n$  colors. In contrast, we form  $n$  binary bit sets,  $\mathcal{Y}_1, \mathcal{Y}_2, \dots, \mathcal{Y}_n$ , by separating each element in  $\mathcal{Y}$  into  $n$  binary indicators, and train  $n$  binary SVMs by using  $\{\mathcal{X}, \mathcal{Y}_1\}, \{\mathcal{X}, \mathcal{Y}_2\}, \dots, \{\mathcal{X}, \mathcal{Y}_n\}$  as separate sets of training data. In this way, the prediction cost scales *linearly* with the number of layers. We use LSVM as a shorthand for SVM trained using this layered strategy hereafter.

We highlight the following two advantages of LSVM over other traditional methods (e.g., QDA and one-vs-all SVM) in decoding HiQ codes:

- **Low processing latency:** One-vs-all SVM requiring  $2^n$  binary SVM classifiers, while LSVM only need  $n$  binary SVM classifiers for decoding  $n$ -layer HiQ codes which is a huge improvement regarding processing latency.
- **Layer separability:** Using LSVM, the classifications of all layers are completely independent. Therefore, in a sequence of scanning of a multi-layer HiQ code, once a layer is decoded it need not be processed anymore, which saves much computational power. In contrast, the predictions of all layers are coupled together in methods like QDA. Thus, even after a layer has been successfully decoded, it will still be redundantly processed until all layers are decoded successfully.

In subsequent sections, we extend QDA and LSVM further to tackle cross-module interference as QDA and LSVM are shown to have superior performance in color predication compared with other methods (see VII-D for detailed results).

### B. Incorporating Cross-Module Interference Cancellation

To address the cross-module interference in high-density HiQ codes, we append the feature of each module—normalized RGB intensities of the central pixel—with that of its four adjacent modules (top, bottom, left and right) to train the color classifier. However, in this way the feature dimension rises from 3 to 15. In real-world mobile applications, computational power is limited and tens of thousands of predictions per second are required to decode a high-capacity HiQ code which usually consists of ten to thirty thousand modules and it usually takes multiple trials until success. Consequently, directly adding the feature from adjacent modules which increases feature dimension can hardly meet the processing latency requirement. For instance, to decode a 3-layer HiQ code, our experiences show that if use QDA as the color classifier, it takes nearly ten seconds for Google Nexus 5 to finish one frame of decoding, which is prohibitively expensive. Moreover, the computational cost grows dramatically as the number of layer increases.

To accelerate the decoding process, we make the following assumption about the cross-module interference based on a simple color mixing rule [21]: *The true color of the central module is a linear combination of presented colors of central module and that of its four neighboring ones*<sup>7</sup>. With this assumption, we firstly cancel the CMI to recover the true

<sup>7</sup>True color means color without cross-module interference and presented color denotes the color perceived by camera. Mathematically, color is represented by a three-dimensional vector in RGB color space.

---

### Algorithm 1: Algorithm for solving QDA-CMI

---

**Input:** The training data  $\{(x_i, y_i)\}$  where

$$y_i \in \{1, \dots, K\}$$

**Output:**  $\{\Sigma_k\}_{k=1}^K, \{\mu_k\}_{k=1}^K$  and  $M$

- 1 Initialize  $M^0 = [1, 0, 0, 0, 0]^T$ ,  $j = 0$ ;
  - 2 **while not convergence do**
  - 3     **for**  $k \in \{1, \dots, K\}$  **do**
  - 4          $\mu_k^{j+1} = \sum_{i:y_i=k} x_i^T M^j / N_k$ ;
  - 5          $\Sigma_k^{j+1} = \sum_{i:y_i=k} (x_i^T M^j - \mu_k)^T (x_i^T M^j - \mu_k) / N_k$ ;
  - 6     Compute  $M^{j+1}$  using Eq. (5);
  - 7      $j = j + 1$ ;
  - 8  $\Sigma_k = \Sigma_k^j, \mu_k = \mu_k^j$ , for all  $k \in \{1, \dots, K\}$  and  $M = M^j$ ;
- 

color (3-dim) of each module which is a fast linear operation. Secondly, we use the 3-dim true color to do prediction instead of the raw concatenated feature (15-dim). In this way, both accuracy and speed can be achieved.

In the following, we represent the color feature  $x_i$  as a  $5 \times 3$  matrix of which each row is formed by the normalized RGB intensities and define  $M$  as a  $5 \times 1$  column vector whose items are weights for the corresponding modules. Thus the true color of the  $i$ th sample

$$\hat{x}_i = x_i^T M. \quad (1)$$

By substituting the training data point,  $\hat{x}_i$ , in the formulation of QDA and LSVM with Eq. (1), we introduce two models—QDA-CMI and LSVM-CMI.

**QDA-CMI.** Using Conventional QDA (without considering CMI), we assume the density function of the *presented color*,  $x_i$ , to be a multivariate Gaussian:

$$f_k(x_i) = \frac{1}{\sqrt{(2\pi)^l |\Sigma_k|}} e^{-\frac{1}{2}(x_i - \mu_k)^T \Sigma_k^{-1} (x_i - \mu_k)}, \quad (2)$$

where  $k$  is the color (class) index,  $l$  is the feature dimension,  $\mu_k$  and  $\Sigma_k$  are the mean vector and covariance matrix of the  $k$ th class, respectively.

To incorporate CMI cancellation, we model the *true color*,  $\hat{x}_i$ , rather than the presented color, as a multivariate Gaussian. Together with Eq. (1), we obtain the following density function:

$$f_k(x_i) = \frac{1}{\sqrt{(2\pi)^l |\Sigma_k|}} e^{-\frac{1}{2}(x_i^T M - \mu_k)^T \Sigma_k^{-1} (x_i^T M - \mu_k)}. \quad (3)$$

We jointly learn the parameters  $\Sigma_k, \mu_k$  and  $M$  using maximum likelihood estimation (MLE) which maximizes the following objective function:

$$G(\Sigma, \mu, M) = \prod_{k=1}^K \prod_{i:y_i=k} f_k(x_i), \quad (4)$$

where  $\Sigma = \{\Sigma_k\}_{k=1}^K$  and  $\mu = \{\mu_k\}_{k=1}^K$ . We solve this problem by alternately optimizing over  $(\Sigma, \mu)$  and  $M$ , see Algorithm 1 for the details. At the first step, we initialize  $M$  such that the element corresponding to the central module to be

1 and others to be 0. Note that with  $M$  fixed, the problem degenerates to traditional QDA and the solution is the MLE of  $K$  multivariate Gaussian distributions:  $\mu_k = \sum_{i:y_i=k} \mathbf{x}_i^\top M / N_k$  and  $\Sigma_k = \sum_{i:y_i=k} (\mathbf{x}_i^\top M - \mu_k)^\top (\mathbf{x}_i^\top M - \mu_k) / N_k$ , where  $N_k$  is number of class- $k$  observations.

At the second step, we fix  $(\Sigma, \mu)$  and optimize  $M$ , which is equivalent to maximizing the log-likelihood function

$$\begin{aligned} \mathcal{L}(\Sigma, \mu, M) &= \log G(\Sigma, \mu, M) \\ &= -\frac{1}{2} \sum_{k=1}^K \sum_{i:y_i=k} (\mathbf{x}_i^\top M - \mu_k)^\top \Sigma_k^{-1} (\mathbf{x}_i^\top M - \mu_k) + C, \end{aligned}$$

where  $C$  is some constant. By taking the derivative of  $\mathcal{L}(\Sigma, \mu, M)$  w.r.t.  $M$  and setting it to zero, we have

$$M = \left( \sum_{k=1}^K \sum_{i:y_i=k} \mathbf{x}_i^\top \Sigma_k^{-1} \mathbf{x}_i \right)^{-1} \left( \sum_{k=1}^K \sum_{i:y_i=k} \mathbf{x}_i^\top \Sigma_k^{-1} \mu_k \right). \quad (5)$$

Then the algorithm alternates between Step one and Step two until convergence.

**LSVM-CMI.** Similarly, we can also model the true color using LSVM by substituting Eq. (1) into the original formulation of LSVM. Therefore, in LSVM-CMI, we train the  $j$ th binary SVM on the training data,  $\Xi_j = \{\mathcal{X}, \mathcal{Y}_j\}$ , by solving the following optimization problem (P1):

$$\min_{\omega_j, b_j, \xi, M_j} \frac{1}{2} \|\omega_j\|^2 + C \sum_{i=1}^N \xi_i \quad (P1)$$

$$\text{s.t. } \omega_j^\top \mathbf{x}_i^\top M_j + b_j \geq 1 - \xi_i \quad \forall (\mathbf{x}_i, y_i = 1) \in \Xi_j, \quad (6)$$

$$\omega_j^\top \mathbf{x}_i^\top M_j + b_j \leq -1 + \xi_i \quad \forall (\mathbf{x}_i, y_i = 0) \in \Xi_j, \quad (7)$$

$$\xi_i \geq 0 \quad 1 \leq i \leq N, \quad (8)$$

$$\mathbf{e}^\top \cdot M_j = 1, \quad (9)$$

where  $\mathbf{e} = \{1, 1, 1, 1, 1\}^\top$ ,  $\xi = (\xi_i | i = 1, 2, \dots, n)$ ,  $1 \leq j \leq n$  and  $N$  is the number of training data points. In this optimization problem, we have made a constraint on  $M_j$  (i.e., Eq. (9)) such that the nonnegative weights of the five modules sum up to one. It can be readily shown that both Constraints (6) and (7) can be represented by one equation as follows:

$$(2y_i - 1)(1 - \xi_i - \omega_j^\top \mathbf{x}_i^\top M_j - b_j) \leq 0. \quad (10)$$

The following lemma characterizes one property of the optimal value of  $W_j$  to the optimization problem P1.

**Lemma 1.**  $W_j^*$ , the optimal value of  $W_j$  for P1, has at most one nonzero element.

*Proof.* Since P1 is a convex program, we can adopt convex optimization techniques to tackle it. To be more specific, we first write down the following Lagrangian function:

$$\begin{aligned} L(\lambda, \omega_j, b_j, \xi, M_j) &= \sum_{i=1}^n \lambda_i (2y_i - 1)(1 - \xi_i - \omega_j^\top \mathbf{x}_i^\top M_j - b_j) \\ &\quad + \frac{1}{2} \|\omega_j\|^2 + C \sum_{i=1}^N \xi_i \end{aligned} \quad (11)$$

where  $\lambda = (\lambda_i | i = 1, 2, \dots, n)$  is the Lagrangian multiplier with respect to Eq. (10). Thus, the dual problem is given by:

$$\begin{aligned} \max_{\lambda} \quad & \min_{\omega_j, b_j, \xi, M_j} L(\lambda, \omega_j, b_j, \xi, M_j) \\ \text{s.t.} \quad & \text{Eq. (8), (9)} \end{aligned} \quad (12)$$

Combine Eq. (9) and Eq. (11), for a fixed  $\lambda$ , the Lagrangian objective is a linear function of  $M_j$  subject to a linear constraint of  $M_j$ . Therefore, for the feasible set, i.e.,  $\{M_j | \mathbf{e}^\top \cdot M_j = 1\}$ , the optimum of the dual problem is obtained at some vertex. This completes the proof.  $\square$

Lemma 1 states that, only a small portion of features can be used to train the SVM model due to the linearity of  $M_j$ . Therefore, we modify Constraint (9) to yield the following equation:

$$M_j^\top M_j \leq 1, \quad (14)$$

where we expand the original feasible set of  $M_j$  to form a sphere. In the sequel, we shall solve the optimization problem subject to the constraint in Eq. (14).

Observe that, on the one hand, for a fixed  $M_j$ , P1 reduces to a standard SVM optimization problem. On the other hand, when  $w_j$  and  $b_j$  are given, P1 is equivalent to the following optimization problem (P2):

$$\min_{M_j} \sum_{i=1}^N \max \left\{ 0, 1 + (1 - 2y_i)(w_j^\top \mathbf{x}_i^\top M_j + b_j) \right\} \quad (P2)$$

$$\text{s.t. } M_j^\top M_j \leq 1. \quad (15)$$

P2 is a constrained optimization problem and we adopt the gradient projection approach [22] to tackle it. Towards this end, we design the following algorithm to solve the optimization problem P1.

---

**Algorithm 2:** Algorithm for solving LSVM-CMI

---

1. Initialize  $M_j = \{1, 0, 0, 0, 0\}$ ;
  2. Repeat the following steps until convergence;
  3. Fix  $M_j$ , apply the dual approach to solve P1, which outputs the local optimal solution  $w_j$ ;
  4. Fix  $w_j$ , apply the gradient projection approach to solve P2, which outputs the local optimal solution  $M_j$ ;
- 

We proceed to characterize the global optimality of Algorithm 2 in the following theorem:

**Theorem 1.** Algorithm 2 converges to the global optimum of P1.

*Proof.* In Algorithm 2, the optimization process in Step 3 and Step 4 can only reduce the objective value, Algorithm 2 converges to a local optimum of P1. Since P1 is a convex optimization problem, its optimal solution is therefore also global optimal. This completes the proof.  $\square$

Theorem 1 states that, Algorithm 2 shall output the optimal solution to P1, i.e.,  $w_j^*$ ,  $b_j^*$  and  $M_j^*$ . So given a testing sample  $\mathbf{x}$ , we use all  $n$  SVMs to output the predicted  $n$ -tuple,  $\hat{\mathbf{y}} = \{\hat{y}_1, \dots, \hat{y}_n\}$ , where

$$\hat{y}_j = \text{sign}((\omega_j^*)^\top \mathbf{x} M_j^* + b_j^*). \quad (16)$$



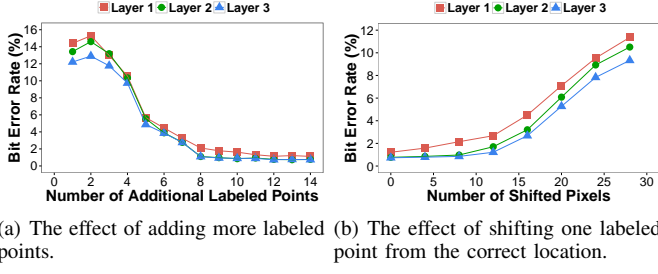


Figure 5: The estimation of the geometric transformation matrix. The module size of the HiQ code under testing is approximately 17 pixels.

Experimental results on 5390 3-layer HiQ codes samples show that CMI cancellation reduces the decoding failure rate by nearly 9% (from 65% to 56%) by reducing the bit error rate from 4.3% to 3.2% averaging over all layers. See Section VII-E for more detailed evaluation which also reveals that CMI cancellation helps to increase the density of HiQ codes. For example, with LSVM-CMI the minimum decodable printout size of a 7700-byte HiQ code is reduced from  $50 \times 50 \text{ mm}^2$  to  $38 \times 38 \text{ mm}^2$  (the density is increased by more than 46%).

## V. ROBUST GEOMETRIC TRANSFORMATION

Standard methods correct geometric distortion by detecting four spatial patterns in the corners of a QR code. However, in practice, the detection is inevitably inaccurate, and the cross-module interference makes the decoding more sensitive to transformation errors caused by inexact detection, especially for high-density QR codes. We find that using more points to calculate geometric transformation reduces the reconstruction error significantly, see Fig. 5(a) for experimental results. Therefore, instead of developing a more complicated detection algorithm which increases processing latency, we address this problem by using a robust geometric transformation (RGT) algorithm which accurately samples for each module a pixel within the central region where the color interference is less severe than that along the edges of a module. Unlike standard methods, RGT leverages all spatial patterns, including the internal ones, and solves a *weighted* over-determined linear system to estimate the transformation matrix.

Given  $N$  tuples each consists of a pair of 2D data-points, namely,  $\{< \mathbf{x}_i, \mathbf{x}_i' >, i = 1, 2, \dots, N\}$ , where  $\mathbf{x}_i$  is the position of a detected pattern, and  $\mathbf{x}_i'$  is the corresponding point in the data matrix to be reconstructed. In perspective projection [4],  $\mathbf{x}_i$  is the homogeneous coordinate representation  $(x_i, y_i, z_i)$  where we empirically choose  $z_i = 1$ , and each pair of corresponding points gives two linear equations:

$$A_i H = \mathbf{0}, \quad (17)$$

where  $H$  is the transformation matrix to be estimated and

$$A_i = \begin{bmatrix} \mathbf{0}^T & -\mathbf{x}_i^T & y_i' \mathbf{x}_i^T \\ \mathbf{x}_i^T & \mathbf{0}^T & -x_i' \mathbf{x}_i^T \end{bmatrix}.$$

Note that although  $H$  has 9 entries,  $h_1, h_2, \dots, h_9$ , since in 2D homographies,  $H$  is defined up to scale, and thus has eight

degrees of freedom and one may choose  $h_9 = 1$ . Therefore, four point coordinates give eight independent linear equations as Eq.(17) which are enough for estimating  $H$ . However, since the estimated positions of the special patterns often contain noise, which implies  $A_i H \neq \mathbf{0}$ , RGT regards the norm  $\|A_i H\|_2$  as the transformation error and minimizes a *weighted* error sum to obtain the estimation of  $H$ :

$$\begin{aligned} & \underset{H}{\text{minimize}} && \sum_{i=1}^N w_i \|A_i H\|_2 \\ & \text{subject to} && \|H\|_2 = 1. \end{aligned} \quad (18)$$

where  $w_i$  is the weighting factor of each input point  $\mathbf{x}_i$ . Instead of arbitrarily fixing one  $h_i$ , we add constraint  $\|H\|_2 = 1$  to avoid  $H = \mathbf{0}$ . As we find that the estimated positions of finder patterns are often more accurate than that of alignment patterns, we assign higher weights to detected positions of finder patterns and lower weights to alignment patterns. Empirically, we set  $w_i = 0.6$  if  $\mathbf{x}_i$  is from the finder pattern,  $w_i = 0.4$  otherwise. Note that solving (18) is equivalent to solve the following unconstrained optimization problem:

$$\underset{H}{\text{minimize}} \quad \frac{\|AH\|_2}{\|H\|_2} \quad (19)$$

where  $A$  is a matrix built from  $\{w_i A_i | i = 1, \dots, N\}$ , and each  $w_i A_i$  contributes two matrix rows to  $A$ . Fortunately, the solution to Eq.(19) is just the corresponding singular vector of the smallest singular value [4]. Singular value decomposition (SVD) can be used to solve this problem efficiently.

As is shown in Fig. 5(b), RGT is robust to *minor* shift in the detected positions, but *not* false positives. To reduce false positives, we take advantage of the color property by coloring each pattern with a specific color in the encoding phase (see Fig. 3). For each detected pattern, we filter out possible false detections by checking whether the color of it is correct or not.

## VI. PERFORMANCE OPTIMIZATION

### A. Local binarization

Existing monochrome QR code decoders usually use image luminance, e.g., the Y channel of the YUV color space, to binarize QR codes. However, directly applying it on color ones can be problematic because some colors (e.g., yellow) have much lower luminance than other colors, which makes some patterns undetectable. To solve this problem, we use a simple but effective method to binarize HiQ codes. Let  $\mathbf{I}$  denotes an image of a HiQ code formatted in the *RGB* color space. We first equally divide it into  $8 \times 8$  blocks. In each block, a threshold is computed for each channel as follows:

$$T_i = \frac{\max(\mathbf{I}_i) + \min(\mathbf{I}_i)}{2}$$

where  $i \in \{R, G, B\}$  and  $\mathbf{I}_i$  is the  $i$ th channel of image  $\mathbf{I}$ . A pixel denoted by a triplet  $(P_R, P_G, P_B)$  is assigned 1 (black) if  $P_i < T_i$  for any  $i \in \{R, G, B\}$ , 0 (white) otherwise.

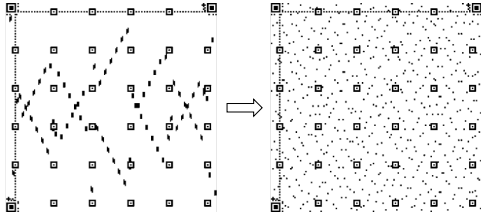


Figure 6: Spatial Randomization of Data Bits. On the left is the bit distribution of the original QR code, and on the right is the bit distribution after randomization.

### B. Spatial randomization and block accumulation

Through our experiences of scanning QR codes using mobile devices, we noticed one strange fact that some localized region somehow causes the entire decoding process to fail even though the bit error rate averaging over the entire QR code should be recoverable by the built-in Reed-Solomon error correcting coding of the QR code. After examining the error correction mechanism, we surprisingly found that QR code decoder performs error correction block by block, and in each data block data is shuffled byte by byte in QR codes. However, for *high-density QR codes*, data bits from the same block do not spread out uniformly. Instead, they tend to assemble in the local areas (see Fig. 6 for illustration). Consequently, the concentration of the data bits in some specific blocks easily leads to error-correction failure because external causes like local overexposure often lead to a large error percentage in one block beyond repair. With even a single block failure, the decoder will initiate a new round of scanning while discarding all information successfully decoded from other blocks. Moreover, most failure decoding cases errors in each captured image always assemble in few blocks instead of affecting all the blocks.

To improve the performance of HiQ framework and reduce scanning latency, we make the following adaptations:

- **Spatial randomization:** To avoid data block decoding failure caused by local error, we propose to shuffle the data of each block bit-by-bit into the whole matrix *uniformly*, which we call as *spatial bits randomization*, to improve the probability of successful correction of each block as shown in Fig. 6.
- **Data block accumulation:** Moreover, in order to prevent the failure in one single block making the efforts in other blocks in vain, we propose *Data Block Accumulation*, which accumulates the successfully decoded data blocks in previous scans until all the data blocks are decoded.

By using these refinements, we manage to cut down the scanning latency significantly, see Section VII-F for experimental results.

## VII. EVALUATION

In this section, we present the implementation details of HiQ and the results of comprehensive experiments. We design two phases of experiments. In the first phase, we compare HiQ with the baseline method on a challenging HiQ code dataset,

CUHK-CQRC. In the second phase, we evaluate HiQ in real-world operation using off-the-shelf mobile devices. In particular, we collect a large-scale HiQ code dataset, CUHK-CQRC, to evaluate the performance of HiQ by comparing with PCCC [2]. Note that PCCC provides two different methods: PB for the HiQ code with embedded reference color and EM for those without using the reference color. In our implementation of PCCC we use PB as PB is reported to outperform EM [2].

### A. Performance Metrics

We use the following three metrics to quantify the performance of each approach: 1) Bit Error Rate (BER), 2) Decoding Failure Rate (DFR), 3) scanning time. DFR and BER are used to measure the evaluation on CUHK-CQRC which is conducted via Matlab simulation in a frame-by-frame manner. Scanning time is used for characterizing the overall user-perceived performance under practical settings.

BER denotes the percentage of wrongly decoded bits *before* applying the built-in Reed-Solomon error correction mechanism; DFR is the percentage of the QR codes that cannot be decoded *after* the error correction mechanism is applied over those that can be successfully localized. DFR measures the overall performance of the decoding method. Compared with DFR, BER is a more fine-grained metric which directly measures the error of the color recovery and the geometric transformation. Scanning time is the interval between the time when the camera takes the first frame and the time when the decoding is successfully completed. It measures the overall performance of the decoding approaches on mobile devices which reflects the user experience.

### B. CUHK-CQRC: A Large-Scale Color QR Code Dataset

We establish a challenging HiQ code dataset, CUHK-CQRC, in this paper. CUHK-CQRC consists of 1,506 photos and 3,884 camera previews (video frames) of high-density 3-layer color QR codes captured by different phone models under different lighting conditions. Fig. 7 presents some samples of CUHK-CQRC. Different from [2], we also include previews in our dataset because of the following two reasons. Firstly, photos are different from previews. When users take a photo using the on-board camera of a mobile phone, many embedded systems implicitly process (e.g., lightweight deblurring and color correction) the output image in order to make it more attractive in appearance, while preview will not go through this process. Secondly, compared with capturing *photos*, it is

Table I: Types of Smartphones Used in Collecting Database

ID	Model Name	Megapixels (MP)	Image Stabilization	Auto-focus
1	iPhone 6 plus	8.0	✓ (optical)	✓
2	iPhone 6	8.0	✓ (digital)	✓
3	Nexus 4	8.0		✓
4	Meizu MX2	8.0		✓
5	Oneplus 1	13.0		✓
6	Galaxy Nexus 3	5.0		✓
7	Sony Xperia M2	8.0		✓
8	Nexus 5	8.0	✓ (optical)	✓





Figure 7: Samples from CUHK-CQRC captured under different lighting conditions.

much faster and more cost-effective for a cellphone camera to generate previews, and hence most mobile applications use camera previews as the input of the decoder.

We implement the HiQ code generator based on an open-source barcode processing library, ZXing. For fair comparison between HiQ and PCCC in which the HiQ code is inherently 3-layer, we generate 5 high-capacity 3-layer color QR codes with different data capacities (excluding redundancies from error correction mechanism) which are 2787 bytes, 3819 bytes, 5196 bytes, 6909 bytes and 8859 bytes (maximum for a 3-layer HiQ code). In order to test the limit of each approach, all color QR codes are embedded with *low* level of error correction in each layer. By using a common color printer (Ricoh Aficio MP C5501A), we print each generated HiQ code on ordinary white paper substrate in different printout sizes, 30 mm, 40 mm, 50 mm and 60 mm (for simplicity, we use the length of one side of the square to represent the printout size), and two different printout resolutions, 600dpi and 1200dpi. To simulate the normal scanning scenario, the samples are captured by different users under several typical lighting conditions: indoor, outdoor (under different types of weather and time of a day), fluorescent, incandescent, and shadowed (both uniform and nonuniform cases are considered). Moreover, we capture the images using eight types of popular smartphones (see Table I for details).

### C. Implementation Details

Although the QR codes in CUHK-CQRC are generated using the proposed encoder (Section III), the color QR codes are also compatible with the PCCC decoder. Both HiQ and PCCC are implemented using the decoder part of a popular monochrome QR code implementation, ZXing codebase [23]. As suggested in Table II, LSVM with different kernels has similar performance in the first two layers, so in our implementation of LSVM and LSVM-CMI, we use linear kernel in the first two layers and polynomial kernel of degree 3 in the third layer to reduce latency.

Since the parameters of HiQ are learned offline, we train the color classifier of HiQ using data sampled from CUHK-CQRC prior to conducting experiments. We select 65 images of color QR codes which cover different lighting conditions, phone models, print resolutions and formats (i.e., photo and preview) for training and use the rest for testing. To collect the color data from the HiQ code images, we use a human-assisted labeling approach. To be more specific, given a captured image of a HiQ code, instead of manually labeling the color pixel by pixel, we only manually input the positions of the markers of

Table II: Color Prediction under Fluorescent Light Accuracy of Different Methods

Method (kernel)	Layer 1	Layer 2	Layer 3	Avg	Time
LSVM (linear)	0.35%	0.66%	4.07%	1.69%	1
SVM (linear)	1.72%	0.71%	3.16%	1.86%	2.7
LSVM (RBF)	0.29%	0.56%	1.85%	0.90%	$\infty$
SVM (RBF)	0.38%	1.68%	2.01%	1.02%	$\infty$
QDA	0.32%	0.60%	1.86%	0.93%	10.7
Decision Forest	0.55%	1.47%	3.07%	1.70%	$\infty$
LSVM (Poly-3)	0.28%	0.57%	2.00%	0.95%	6.7
LSVM (Poly-2)	0.32%	0.59%	2.60%	1.17%	3.3

" $\infty$ " means the algorithm is too heavy-weight for mobile implementation.

the HiQ code and apply the existing geometric transformation algorithm to sample the color data from each square module of which we actually know the ground-truth color. In this way, we can substantially cut down the manual labeling effort while managing to collect over 0.6 million of labeled color-data modules under a wide range of real-world operating/lighting conditions. Such a rich set of labeled data plays an important role in boosting color classification performance for our learning-based decoding algorithm.

### D. Comparing Different Color Classifiers

In this section, we evaluate the color recovery performance of different machine learning techniques, including LSVM (without incorporating CMI cancellation), one-vs-all SVM, QDA [24] and decision forests [25] on real-operating color data (one million pixel samples). Table II presents the results. Linear, polynomial (of degree 2 and 3, denoted as Poly-2 and Poly-3, respectively) and RBF kernels are tried in SVM implementation. For random forests, we use depth-9 trees and train 100 of them by using 5 random splits when training each weak learner. According to Table II, Layered SVM with RBF kernel appears to be the best choice for our application considering accuracy, but using kernel techniques in SVM on a mobile application is too time-consuming. Alternatively, one can either approximate the RBF kernel via explicit feature mapping [26] [27], or map the original feature into a slightly higher dimensional space using an as-good kernel such as a low-degree polynomial kernel [28]. For decoding quickness, we choose the latter in our implementation. Considering speed and accuracy, QDA and LSVM (Poly-3) are more favorable than others. Between QDA and LSVM, QDA is of higher accuracy while LSVM has lower processing latency.

### E. Evaluation of HiQ on CUHK-CQRC

In section, we evaluate the performance of HiQ by comparing it with the baseline method, PCCC from [2], using

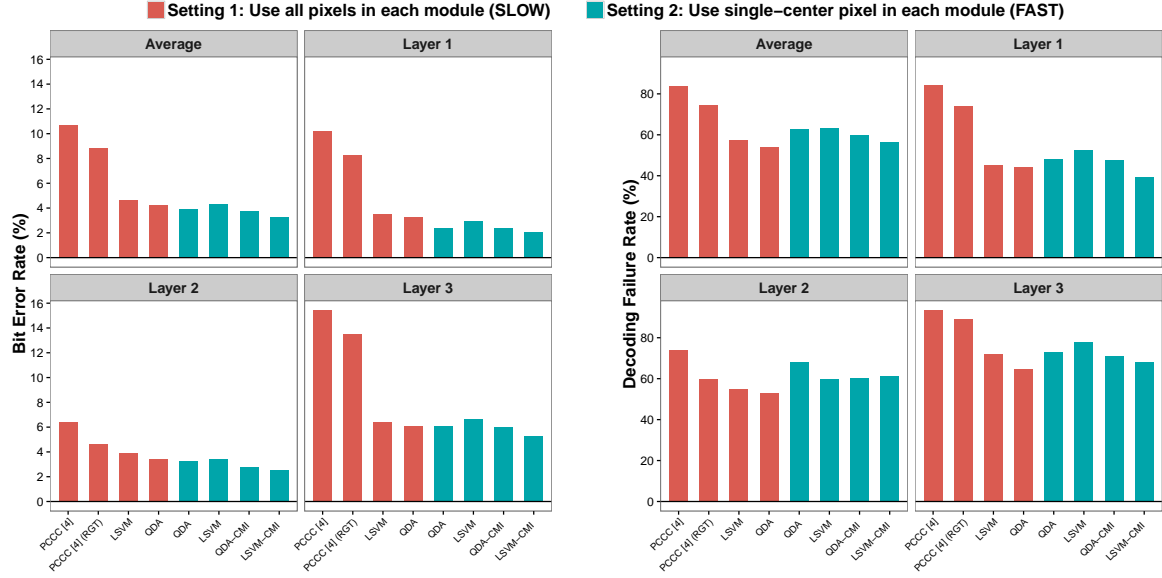


Figure 8: Bit error rate (left) and decoding failure rate (right) of different color recovery methods on CUHK-CQRC. **Setting 1:** four color recovery methods (PCCC [2], PCCC with RGT, QDA and LSVM) are performed on every pixel of a captured image. **Setting 2:** four color recovery methods (QDA, LSVM, QDA-CMI and LSVM-CMI) are performed only on the center pixel of each color module.

CUHK-CQRC. Since PCCC performs color recovery on each pixel of a captured image before applying local binarization (Setting 1), while in the proposed QDA-CMI and LSVM-CMI we only perform color recovery on the center pixel of each color module (Setting 2). Performing color recovery on every pixel helps decoding because binarization can benefit from neighboring pixels, but it is prohibitively time-consuming for practical consideration as a captured image usually consists of more than one million pixels. For fair comparison, we conduct two groups of experiments under the above two settings. In Setting 1, we compare PCCC with HiQ which uses QDA and LSVM (Poly-3) as the color classifier to show that our framework actually beats the baseline even without adopting CMI cancellation techniques. In Setting 2, by comparing QDA-CMI and LSVM-CMI with QDA and LSVM, we show the superiority of the proposed QDA-CMI and LSVM-CMI.

The results presented in Fig. 8 show that, in Setting 1, HiQ with QDA reduces BER from 10.7% to 4.3% and DFR from 84% to 54% (the decoding success rate is increased by 188%) compared with PCCC. Moreover, we also apply robust geometric transformation (RGT) on PCCC, denoted as *PCCC (RGT)*. RGT is shown to reduce the DFR and BER of PCCC by 12% and 18%, respectively. As for QDA and LSVM, they are comparable in decoding performance as also indicated in Table II. The results also indicate that, across all of the 3 schemes under test, the third layer (yellow channel in PCCC) always yields the worst performance. This is because the color classifier has poor performance in distinguishing between yellow and white which are encoded as 001 and 000 respectively in the codebook (see Fig. 3), especially under strong light. Likewise, the classifier performs poorly in distinguishing blue (110) and black (111) under dim light. The combined effect is that the third layer often cannot be

decoded reliably during poor lighting conditions. Fortunately, it is possible to apply a higher error correction level on the third layer to compensate for the higher classification error rate, which will be investigated in Section. VII-F.

In Setting 2, both QDA-CMI and LSVM-CMI models outperform their base models (QDA and LSVM) in both DFR and BER. In particular, LSVM-CMI reduces the BER of LSVM by 16.8% while QDA-CMI reduces the BER of QDA by 6.8%. Compared with LSVM-CMI, the performance of QDA-CMI is inferior and QDA-CMI is shown to have less significant improvement over its base model. This is probably due to the fact that the objective function of QDA-CMI (see Eq. (4)) is in general non-convex while the objective of LSVM-CMI is convex. Consequently, the optimization of QDA-CMI (Algorithm 1) is likely to be stuck at a local optimum and yields a suboptimal solution. Yet another limitation of QDA-CMI is that the data points lying along the edges of the Gaussian distribution unfavorably affect the optimization. In other words, a small number of data points can significantly change the value of the objective function while having negligible effects on reducing the prediction error.

Although the overall decoding failure rate of our method (over 50%) may look high, if one frame fails, the smartphone can instantly capture a new image and start a new round of decoding until the QR code is successfully decoded. Therefore, besides accuracy, processing latency also serves as a key aspect in measuring the practicability of one approach. In the following, we will study the performance of different methods in real-world practice, considering both accuracy and processing latency.

#### F. Evaluation of HiQ on Mobile Devices

In this section, we demonstrate the effectiveness of HiQ using off-the-shelf smartphones, which include Google Nexus

Table III: Scanning Performance of Different Color Recovery Algorithms using iPhone 6s Plus

		QDA	LSVM	QDA-CMI	LSVM-CMI
<b>3819 bytes</b> <b>35 × 35 mm<sup>2</sup></b>	Number of frames	1.44	1.86	1.31	1.13
	Overall latency (ms)	375.06	372.83	372.49	264.29
	Time per frame (ms)	260.91	200.22	283.41	234.09
<b>5196 bytes</b> <b>40 × 40 mm<sup>2</sup></b>	Number of frames	1.40	1.44	1.33	1.33
	Overall latency (ms)	435.32	308.36	479.33	365.16
	Time per frame (ms)	310.94	214.14	359.50	275.47
<b>6909 bytes</b> <b>50 × 50 mm<sup>2</sup></b>	Number of frames	3.65	5.51	1.61	1.24
	Overall latency (ms)	1323.77	1295.17	670.13	401.24
	Time per frame (ms)	362.30	234.75	415.48	323.81
<b>8097 bytes</b> <b>38 × 38 mm<sup>2</sup></b>	Number of frames	-	-	-	4.80
	Overall latency (ms)	-	-	-	2146.23
	Time per frame (ms)	-	-	-	447.13

“-” means cannot be successfully decoded.

5, iPhone 6 Plus and iPhone 7 Plus. We investigate several interesting questions: 1) Compared with QDA, LSVM is superior in speed but inferior in accuracy (see Table II), so how their performance differs in real-world mobile applications; 2) How different color recovery methods proposed in this paper—QDA, LSVM, QDA-CMI and LSVM-CMI—perform in real-world scenario; 3) What is the impact of different error correction levels on the performance of HiQ; and 4) How the decoding performance varies with respect to the physical printout size of HiQ codes. As evaluation metrics, we collect the scanning time of 30 successful scans (i.e., trials where the HiQ code is successfully decoded) for each printout HiQ code and the experiments are conducted in an indoor office environment. A trial is unsuccessful if the code cannot be decoded within 60 seconds, and a HiQ code is regarded as *undecodable* if three consecutive unsuccessful trials occur.

Table III lists the experimental results of different color recovery algorithms in real-world mobile applications by using iPhone 6s Plus as representative. In this experiment, we select several challenging HiQ codes samples of low level of error correction in all layers, different data capacities (3819 bytes, 5196 bytes, 6909 bytes and 8097 bytes) and different printout sizes ( $35 \times 35 \text{ mm}^2$ ,  $40 \times 40 \text{ mm}^2$ ,  $50 \times 50 \text{ mm}^2$  and  $38 \times 38 \text{ mm}^2$ ). The results show that LSVM takes less time to successfully decode a HiQ code compared to QDA (although LSVM takes more frames to complete decoding a HiQ code, it consumes less time to process a frame). By incorporating CMI cancellation, QDA-CMI and LSVM-CMI reduce the overall latency and the increase of computation time for processing a frame is negligible. More importantly, LSVM-CMI achieves the best performance among all methods. In particular, LSVM-CMI has the lowest overall latency and is the only method that can decode the most challenging HiQ code (8097 bytes,  $38 \times 38 \text{ mm}^2$ ) with reasonable computational cost.

In the following, we evaluate the performance of LSVM and LSVM-CMI and show the effectiveness of HiQ and superiority of LSVM-CMI over LSVM in real-world practice. We conduct experiments using 3-layer HiQ codes with different error correction levels and different content sizes using iPhone 6 Plus and iPhone 7 Plus. More specifically, we choose six different content sizes, 2000 bytes, 2900 bytes, 4500 bytes, 6100 bytes, 7700 bytes and 8900 bytes (approximately). For each content size, we generate color QR codes using four

different levels of error correction which are denoted by 4 triplets, LLL, LLM, LLQ and MMM<sup>8</sup>. Each symbol (L, M and Q) of the triplet represents different level of error correction (low, median and quartile<sup>9</sup>) applied for the corresponding layer. We try different error correction levels in the third layer as it has shown to be the most error-prone layer (see Table II). Each generated HiQ code is printed in different printout sizes ranging from 22 mm to 70 mm.

The results presented in Fig. 9 show that HiQ decoder can, in most of the cases, successfully decode the HiQ code within 5 seconds with small variance (see the supplement for more detailed results). Fig. 9 also conveniently shows the smallest printout sizes of the color QR codes with different content sizes that can be decoded in a reliable and rapid manner. Comparing the performance of different error correction levels, we can see that, in most cases, LLL and LLM outperform LLQ and MMM in terms of the smallest decodable printout size given the same content size. This suggests that it is not helpful to apply error correction level that is higher than  $M$  since higher level of error correction not only increases the error-tolerant ability, but also increases the data density by adding more redundancies. More importantly, the comparison between the first two rows of Fig. 9 demonstrates the effectiveness of the proposed CMI cancellation. In particular, LSVM-CMI not only outperforms LSVM in overall scanning latency, but also in minimum decodable printout size of the HiQ codes, e.g., with LSVM-CMI reduces the minimum printout size of 7700-byte HiQ code by 24% (from 50 mm to 38 mm). Fig. 9(a) (iPhone 6 Plus) and Fig. 9(c) (iPhone 7 Plus) suggest that HiQ with LSVM-CMI can achieve similar performance using different mobile devices.

Lastly, we evaluate the performance of spatial randomization for HiQ (see Section VI-B) on mobile device. Using Nexus 5 as a representative phone model, we compare the decoding performance on randomized and non-randomized HiQ codes of different content sizes and printout sizes. Specifically, we choose 6100-byte and 7700-byte HiQ code samples to do the evaluation. Fig. 10 presents the block accumulation

<sup>8</sup>Since data capacity of a QR code will be reduced if higher error correction level is used, we cannot apply 4 different error corrections for all content sizes. For instance, with a content size of 8900 bytes, we can only use LLL, and for content size of 7700 bytes, only LLL and LLM are feasible.

<sup>9</sup>Low, median and quartile level of error correction can correct up to 7%, 15% and 25% codewords, respectively.



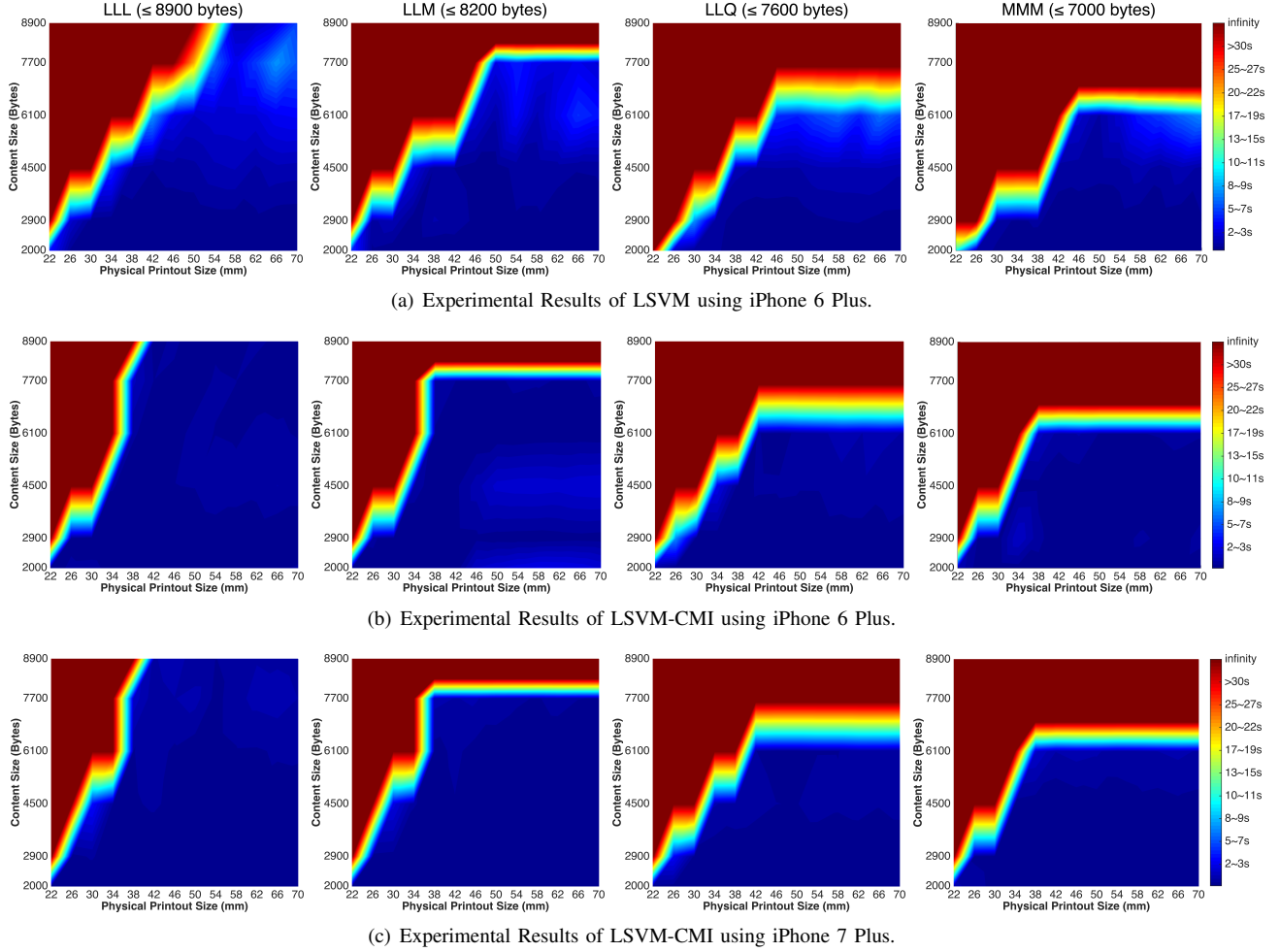


Figure 9: The 90th percentile of the scanning time of 30 trials (in ascending order). From left to right, the four columns use HiQ codes of different error correction levels—LLL ( $\leq 8900$  bytes), LLM ( $\leq 8200$  bytes), LLQ ( $\leq 7600$  bytes), MMM ( $\leq 7000$  bytes), respectively. The scanning time of the HiQ codes beyond its maximal capacity is set to infinity.

Table IV: Execution Time of Basic Blocks in the Pipeline of HiQ Decoder using Nexus 5

Number of Modules	Type	Data Capacity	YUV-2-RGB	Binarization	Patterns Detection	Transformation	Color Recovery	Randomization	Error Correction	Time per Frame	Number of Frames
$137 \times 137$	B/W	1732 bytes	NA	<b>110ms</b> (34%)	<b>112ms</b> (34%)	23ms (7%)	NA	20ms (6%)	41ms (13%)	322ms	3.0
	Color	5196 bytes	<b>400ms</b> (27%)	204ms (14%)	153ms (10%)	14ms (1%)	<b>500ms</b> (34%)	45ms (3%)	150ms (10%)	1466ms	4.5
$157 \times 157$	B/W	2303 bytes	NA	<b>104ms</b> (27%)	<b>123ms</b> (32%)	37ms (10%)	NA	38ms (10%)	60ms (16%)	380ms	4.3
	Color	6909 bytes	<b>386ms</b> (24%)	200ms (12%)	150ms (9%)	20ms (1%)	<b>650ms</b> (40%)	69ms (4%)	160ms (10%)	1635ms	6.7
$177 \times 177$	B/W	2953 bytes	NA	<b>112ms</b> (25%)	<b>138ms</b> (30%)	37ms (8%)	NA	50ms (11%)	97ms (21%)	455ms	5.6
	Color	8859 bytes	<b>400ms</b> (20%)	193ms (10%)	213ms (11%)	25ms (2%)	<b>881ms</b> (44%)	111ms (5%)	200ms (10%)	2023ms	9.0

behavior when decoding HiQ codes with and without randomization. One can observe that the randomized samples have higher starting point of successful blocks percentage and higher accumulation speed, while the decoding of the original samples easily fails. We also found that randomization also improves the decodability of HiQ codes, especially high-capacity ones. For instance, for 6600-bytes HiQ codes, the use of randomization pushes the minimum decodable printout size from 46mm to 42mm, and cuts down the average scanning

latency by over 50% given certain printout sizes.

### G. Pipeline Analysis

We examine the execution time of sequential flows (basic blocks) in the pipeline of our proposed HiQ framework by using single-layer (monochrome) and 3-layer HiQ codes. Specifically, we choose three different versions of QR codes which consist of  $137 \times 137$ ,  $157 \times 157$  and  $177 \times 177$  modules, respectively. For each HiQ code, we evaluate the execution

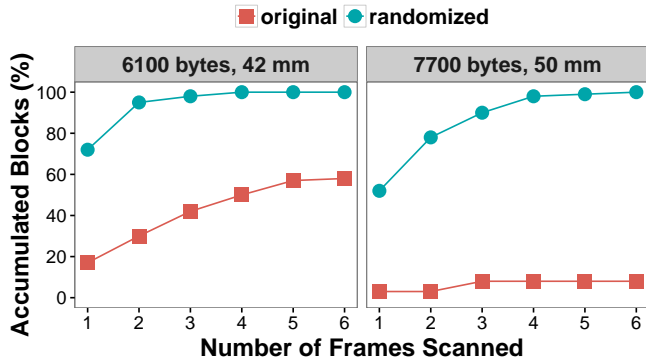


Figure 10: Comparison of scanning performance with respect to block accumulation and randomization.

time of each block by averaging 10 scans using Google Nexus 5.

Observed from Table IV that, the most time-consuming parts for HiQ is color recovery and the YUV-to-RGB conversion, taking up around 40% and 20% respectively. Note that YUV-to-RGB conversion is a necessary step for the implementation on Android to transfer the captured image format from YUV to RGB, but not for iOS. Besides, the randomization part only takes up no more than 11% (120ms) of the scanning time for both single-layer and 3-layer HiQ codes, which is acceptable in practice.

## VIII. CONCLUSION

In this paper, we have proposed two methods that jointly model different types of chromatic distortion (cross-channel color interference and illumination variation) together with newly discovered chromatic distortion, cross-module color interference, for high-density color QR codes. A robust geometric transformation method is developed to address the challenge of geometric distortion. Besides, we have presented a framework for high-capacity color QR codes, HiQ, which enables users and developers to create generalized QR codes with flexible and broader range of choices of data capacity, error correction and color, etc. To evaluate the proposed approach, we have collected the first large-scale color QR code dataset, CUHK-CQRC. Experimental results have shown substantial advantages of the HiQ over the baseline approach. Our implementation of HiQ on both Android and iOS and evaluation using off-the-shelf smartphones have demonstrated its usability and effectiveness in real-world practice. In the future, as opposed to current design where error correction is performed layer by layer, a new mechanism will be developed to share correction capacity across layers by constructing error correction codes and performing correction for all layers as a whole, by which we think the robustness of our color QR code system will be further improved.

## REFERENCES

- [1] Z. Yang, Z. Cheng, C. C. Loy, W. C. Lau, C. M. Li, and G. Li, "Towards robust color recovery for high-capacity color qr codes," in *Proc. IEEE Int. Conf. Image Process. (ICIP)*, Sept. 2016, pp. 2866–2870.
- [2] H. Blasinski, O. Bulan, and G. Sharma, "Per-colorant-channel color barcodes for mobile applications: An interference cancellation framework," *IEEE Trans. Image Process.*, vol. 22, no. 4, pp. 1498–1511, Apr. 2013.

- [3] C. M. Li, P. Hu, and W. C. Lau, "Authpaper: Protecting paper-based documents and credentials using authenticated 2D barcodes," in *IEEE Int. Conf. Commun. (ICC)*, Jun. 2015, pp. 7400–7406.
- [4] R. Hartley and A. Zisserman, *Multiple view geometry in Computer Vision*. Cambridge university press, 2003.
- [5] A. Gijsenij, T. Gevers, and J. Van De Weijer, "Improving color constancy by photometric edge weighting," *IEEE Trans. Pattern Anal. Mach. Intell.*, vol. 34, no. 5, pp. 918–929, May 2012.
- [6] A. Grillo, A. Lentini, M. Querini, and G. F. Italiano, "High capacity colored two dimensional codes," in *Proc. IEEE Int. Multiconf. Comput. Sci. Inf. Technol.*, Oct. 2010, pp. 709–716.
- [7] H. Kato, K. T. Tan, and D. Chai, "Novel colour selection scheme for 2D barcode," in *Proc. IEEE Int. Symp. Intell. Signal Process. Commun. Syst.*, Jan. 2009, pp. 529–532.
- [8] T. Onoda and K. Miwa, "Hierarchised two-dimensional code, creation method thereof, and read method thereof," *available at Japan Patent Office*, vol. 213336, 2005.
- [9] D. Parikh and G. Jancke, "Localization and segmentation of a 2D high capacity color barcode," in *IEEE Workshop Appl. of Comput. Vis. (WACV)*, Jan. 2008, pp. 1–6.
- [10] M. Querini and G. F. Italiano, "Color classifiers for 2D color barcodes," in *Proc. IEEE Fed. Conf. Comput. Sci. and Inf. Syst.*, Sept. 2013, pp. 611–618.
- [11] C. Chen, W. Huang, B. Zhou, C. Liu, and W. H. Mow, "Picode: A new picture-embedding 2d barcode," *IEEE Trans. Image Process.*, vol. 25, no. 8, pp. 3444–3458, Aug. 2016.
- [12] T. Hao, R. Zhou, and G. Xing, "Cobra: color barcode streaming for smartphone systems," in *Proc. ACM 10th Int. Conf. Mobile syst., appl., serv. (MobiSys)*, Jun. 2012, pp. 85–98.
- [13] W. Hu, J. Mao, Z. Huang, Y. Xue, J. She, K. Bian, and G. Shen, "Strata: layered coding for scalable visual communication," in *Proc. ACM 20th annual Int. Conf. Mobile comput. netw. (MobiCom)*, Sept. 2014, pp. 79–90.
- [14] F. Hermans, L. McNamara, G. Sörös, C. Rohner, T. Voigt, and E. Ngai, "Focus: Robust visual codes for everyone," in *Proc. ACM 14th Annual Int. Conf. Mobile syst., appl., serv. (MobiSys)*, Jun. 2016, pp. 319–332.
- [15] H. Bagherinia and R. Manduchi, "A theory of color barcodes," in *IEEE Int. Conf. Comput. Vis. Workshops (ICCV Workshops)*, Nov. 2011, pp. 806–813.
- [16] T. Shimizu, M. Isami, K. Terada, W. Ohyama, and F. Kimura, "Color recognition by extended color space method for 64-color 2-d barcode," in *MVA*, Jan. 2011, pp. 259–262.
- [17] H. Bagherinia and R. Manduchi, "A novel approach for color barcode decoding using smart phones," in *Proc. IEEE Int. Conf. Image Process.*, Oct. 2014, pp. 2556–2559.
- [18] D. Cheng, B. Price, S. Cohen, and M. S. Brown, "Effective learning-based illuminant estimation using simple features," in *Proc. IEEE Conf. Comput. Vis. and Pattern Recognit. (CVPR)*, Oct. 2015, pp. 1000–1008.
- [19] W. Shi, C. C. Loy, and X. Tang, "Deep specialized network for illuminant estimation," in *Eur. Conf. Comput. Vis.*, 2016, pp. 371–387.
- [20] C.-W. Hsu and C.-J. Lin, "A comparison of methods for multiclass support vector machines," *IEEE Trans. Neural Netw.*, vol. 13, no. 2, pp. 415–425, Mar. 2002.
- [21] L. Simonot and M. Hébert, "Between additive and subtractive color mixings: intermediate mixing models," *J. Opt. Soc. Am. A Opt. Image Sci. Vis.*, vol. 31, no. 1, pp. 58–66, Jan. 2014.
- [22] D. Bertsekas, *Nonlinear Programming*. Athena Scientific, 1999.
- [23] A. Mackintosh, A. Martin, B. Brown, C. Brunschen, and S. Daniel, "Zxing. open source library to read 1D/2D barcodes," 2012.
- [24] S. Srivastava, M. R. Gupta, and B. A. Frigiyik, "Bayesian quadratic discriminant analysis," *J. Mach. Learn. Res.*, vol. 8, no. 6, pp. 1277–1305, Dec. 2007.
- [25] A. Criminisi, J. Shotton, and E. Konukoglu, "Decision forests for classification, regression, density estimation, manifold learning and semi-supervised learning," *Microsoft Research Cambridge, Tech. Rep. MSRTR-2011-114*, vol. 5, no. 6, p. 12, 2011.
- [26] A. Rahimi and B. Recht, "Random features for large-scale kernel machines," in *Advances in neural Information processing systems*, 2007, pp. 1177–1184.
- [27] A. Vedaldi and A. Zisserman, "Efficient additive kernels via explicit feature maps," *IEEE Trans. Pattern Anal. Mach. Intell.*, vol. 34, no. 3, pp. 480–492, Mar. 2012.
- [28] Y.-W. Chang, C.-J. Hsieh, K.-W. Chang, M. Ringgaard, and C.-J. Lin, "Training and testing low-degree polynomial data mappings via linear svm," *J. Mach. Learn. Res.*, vol. 11, pp. 1471–1490, Apr. 2010.